ACS APPLIED ENERGY MATERIALS

www.acsaem.org Article

Phase Transitions and Phonon Mode Dynamics of $Ba(Cu_{1/3}Nb_{2/3})O_3$ and $Sr(Cu_{1/3}Nb_{2/3})O_3$ for Understanding Thermoelectric Response

Myung-Eun Song,* Deepam Maurya, Yifei Wang, Jue Wang, Min-Gyu Kang, David Walker, Pam A. Thomas, Scott T. Huxtable, Robert J. Bodnar, N. Q. Vinh,* and Shashank Priya*

Cite This: *ACS Appl. Energy Mater.* 2020, 3, 3939−3945 Read Online

ACCESS | Metrics & More | Article Recommendations | Supporting Information

ABSTRACT: We report electrical and thermal properties of perovskite-type $Ba(Cu_{1/3}Nb_{2/3})O_3$ (BCN) and $Sr(Cu_{1/3}Nb_{2/3})O_3$ (SCN). The BCN and SCN ceramics were synthesized by using the conventional solid state (CS) reaction method. The transmission electron microscopy analysis exhibited needle- and comb-type domain structures in BCN. Interestingly, SCN did not exhibit domain structure; however, it exhibited superlattice reflections due to ordering that were quite prominent in the selected area electron diffraction patterns. The temperature dependence of the dielectric response for BCN and SCN systems exhibits peaks due to structural phase transitions. The change in the Raman modes with increasing temperature also indicated the presence of phase transition in the temperature range 300−400 °C. BCN exhibited a lower value of the thermal conductivity (1.6 W/m·K at 600 °C) as compared to that of SCN (2.1 W/m·K at 600 °C) because of multiple phonon modes as identified through terahertz frequency domain spectroscopy.

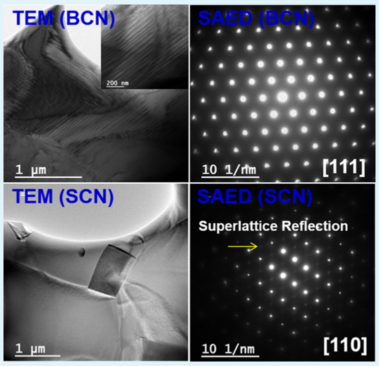

KEYWORDS: *perovskite, domain structure, phase transition, phonon mode, thermal transport, THz frequency domain spectroscopy*

1. INTRODUCTION

Over the past decade there has been significant interest and effort in the development of renewable energy sources (solar, wind, hydroelectric, geothermal power, etc.) as alternatives to fossil fuels.[1−4] Several viable energy materials have been considered to effectively meet the demands for providing sustainable supply of clean, renewable, and affordable energy. Out of several various alternatives, perovskite-based materials have been found to be rather promising due to their intriguing performance in photovoltaics, supercapacitors, batteries, solid oxide cells, and other energy conversion and storage devices.[5−9] The perovskite material family consists of perovskite oxides and organo halide perovskites. In particular, perovskite oxides have attracted considerable attention due to their interesting electrical properties such as ferroelectricity, piezoelectricity, semiconductivity, superconductivity, and ion conductivity.[10] The perovskite oxide (ABO_3) structure comprises close-packed AO_3 , where B-site cations occupy the BO_6 octahedra.[11] In this structure, A-site cations are coordinated by 12 oxygen anions because of the similar size of the oxygen anion. The B-site cations are surrounded by six oxygen anions, and the size of B-site cations is smaller than that of the oxygen anions.[12] Typically, alkaline earth metals and rare earth elements occupy A-sites and transition metals occupy B-sites. As an example of practical perovskites, ferroelectric $BaTiO_3$ and $PbTiO_3$, dielectric $(Ba,Sr)TiO_3$, and multiferroic $BiFeO_3$ have been widely studied because of their technological importance. In many cases, the B-sites with variable valence are beneficial for electron transfer during electrochemical reactions. This allows perovskite-based materials to be considered as new electrode materials for efficient energy storage devices. Because of large tunability in composition, shape, and functionalities, perovskite oxides are promising for renewable and sustainable energy applications.

Perovskite oxides are characterized by a tolerance factor (t), which is defined as

$$t = (R_A + R_B)/1.414(R_B + R_O)$$

where R_A, R_B, and R_O indicate the radius of A-site, B-site, and oxygen ions. When the tolerance factor is around 1.0, the perovskite phase is is considered to have high stability. Using Shannon's ionic radii, BCN and SCN exhibit tolerance factors of 1.03 and 0.97, respectively.[13] For the A-site, the (100) direction of the A cation off-center displacements and the (110) direction of the A−O bonds have an angle of ∼45°. In this case, a tetragonal strain results in relatively small changes in the A−O bond length and its bond order.[14] Both BCN and SCN have tetragonal structure distorted by the Jahn−Teller effect of Cu^{2+}.[15] BCN shows a stable tetragonal distortion at room temperature with a perceived high tetragonality of 3.5%.

Received: February 16, 2020
Accepted: March 30, 2020
Published: April 13, 2020

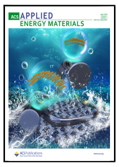

https://dx.doi.org/10.1021/acsaem.0c00342
ACS Appl. Energy Mater. 2020, 3, 3939−3945

It also has a Curie temperature (T_C) around 600 °C where the structure changes to a cubic phase.[16] Venevtsev has reported that BCN is a ferroelectric compound with $T_C = 370$ °C.[17] On the other hand, Zhang et al. reported that BCN showed the maximum dielectric constant around 80000 at 520 °C where the phase transition occurred from tetragonal to cubic symmetry.[18] In the case of SCN, the larger distortion is attributed to smaller Sr^{2+}, which can cause cooperative buckling of the corner-shared octahedron.[19] SCN is also reported to be a ferroelectric compound with $T_C = 380$ °C.[20] Rao et al. investigated dielectric properties of SCN and reported the peak dielectric constant of 255 at 345 °C where the phase transition occurred.[21] The phase transition behavior in these materials is not well understood. Over the past few decades, perovskite-type BCN and SCN ceramics have been studied due to their potential ferroelectric/piezoelectric properties as lead-free ceramics. These materials also exhibited low electrical resistance at high temperature with low thermal conductivity, which makes them interesting for high-temperature oxide thermoelectric applications. The literature on understanding of the transport properties (electrical and thermal) is limited for these materials.

In this paper, we investigate the phase transition characteristics and phonon mode dynamics of perovskite-type BCN and SCN. The fundamental understanding achieved in this work will be helpful for designing novel perovskite materials for harvesting waste thermal energy and other applications.

2. RESULTS AND DISCUSSION

2.1. Phase Composition and Microstructure.

The XRD patterns of the BCN and SCN samples revealed their crystallization in perovskite phase, as shown in Figure S1a,b. BCN ceramics sintered at 1150 and 1250 °C were crystallized in perovskite phase; however, single phase was not found in the calcined powder. A secondary phase was evident in the calcined powder and in the sample sintered at 1200 °C. The *c*/*a* ratio for the BCN ceramics sintered at 1250 °C was found to be 1.035. In the case of SCN, the tetragonal phase was not synthesized in the calcined powder, but all of the sintered samples were crystallized in perovskite phase with an apparent tetragonal symmetry. Because small Sr^{2+} can cause cooperative buckling of the corner-shared octahedron which leads to the larger distortion in SCN,[19] the tetragonality of SCN is much higher (~3%) than that of $BaTiO_3$ (~1%).

Figure S2 shows the SEM images of BCN and SCN ceramics sintered at various temperatures in the range 1150−1400 °C for 2 h. The average grain size of BCN was found to gradually increase from 0.3−3 μm with increasing temperature. As shown in Figure S2a, high-density BCN samples were achieved. The density estimated by using Archimedes' method for the BCN pellet sintered at 1250 °C was >95% of the relative density.

Figure S2b shows the SEM images of SCN samples sintered at 1300−1400 °C. Optimization of the sintering temperature was performed to obtain dense microstructure for SCN ceramics. The average grain size of SCN was found to increase dramatically from 0.5 to 6 μm within a narrow temperature range of 1300−1400 °C. One sample revealed the presence of some liquid phase in the micrographs of the SCN, sintered at 1400 °C, due to the low melting temperature of CuO (~1326 °C). The relative density of the SCN sample, sintered at 1350 °C, was found to be 97%.

As shown in the histogram in Figure S2, the grain sizes of BCN and SCN ceramics increase with sintering temperature. In terms of thermodynamic factors, the grain growth equation is given by

$$G^m = G_0^m + Kt$$

where K is a temperature-dependent growth factor, G is the grain size, and G_0 is the initial grain size ($G = G_0$ at $t = 0$). The value $m = 2$ indicates the rate-controlling variable is diffusion while the value $m = 3$ indicates the rate-controlling variable is interfacial reaction. Based on the Arrhenius relation $K = K_0 \exp(-Q/RT)$, where K_0 is a constant, Q is the activation energy for grain growth, and R is the gas constant, the growth factor K depends on temperature T which leads to variation of the grain size G in the grain growth equation. The relatively larger grains in BCN and SCN at higher sintering temperature were consistent with this relation.

The domain structure of BCN was investigated by using bright-field TEM images. The ferroelastic lamellar domains having planar nanodomain walls can be observed in Figure 1a. The magnified view of domains having domain walls with thickness ~10−20 nm is shown in the inset of Figure 1a. During phase transitions, the twin domains are formed due to the transformation from a higher symmetry phase to a lower symmetry phase, and the interaction between domain walls results in the formation of a comb pattern as shown in Figure 1b.[22] The domain patterns are hierarchical because of the fact that they can be decomposed into simpler patterns until the most elementary unit "domain wall" is found.[22] Figure 1b and the inset of Figure 1a show that TEM images of the domain structures at nanoscale and the corresponding selected area electron diffraction (SAED) patterns are shown in Figures 1d and 1c, respectively. The splitting of diffraction spots in SAED (Figure 1d) shows an existence of nanodomains with domain walls crossed at an angle of ~90°, indicating a comb-type domain structure compared to diffraction spots in Figure 1c that correspond to needle-type domain structure.

Figures 1e and 1f show bright-field TEM images of SCN. Unlike BCN, no domain structure was observed in SCN, as it only exhibited microstructure having grains and grain boundaries. Figures 1g and 1h show SAED patterns from SCN, and the superlattice reflections due to ordering were more prominent in the SAED patterns from other zone axis. The ordering of B-site ions can take place when there is more than one kind of ion in the B-site. Large differences in size and charge between the B-site ions resulted in the ordering of B ions.[23,24] In the case of SCN, the B-site consists of two different cations: Cu^{2+} and Nb^{5+}. The differences in size and charge were enough to lead to ordering, facilitated by the distortion created by smaller Sr^{2+} substitution at the A-site. The 1:2 ordering of B-site ions results in the 3-fold enlarging of the unit cell of SCN.[12] The contribution of the octahedral tilting to these superlattice reflections also cannot be ruled out.

2.2. Phase Transition Characteristics of BCN and SCN.

In the case of isovalent substitution of A-site, Ba and Sr have different ionic radii which can affect structures of BCN and SCN. Compared to the relatively larger size of Ba (ionic radius = 1.35 Å), smaller Sr (ionic radius = 1.18 Å) could lead to reduced repulsive interaction with B-site cation.[25] The schematic view of the crystalline structure of $A(Cu_{1/3}Nb_{2/3})O_3$ (A = Ba, Sr) and partial substitution of Ba/Sr on A sites in the perovskite structure is provided in Figure S3. According to first-principles studies, smaller size ions tend to shift to off-

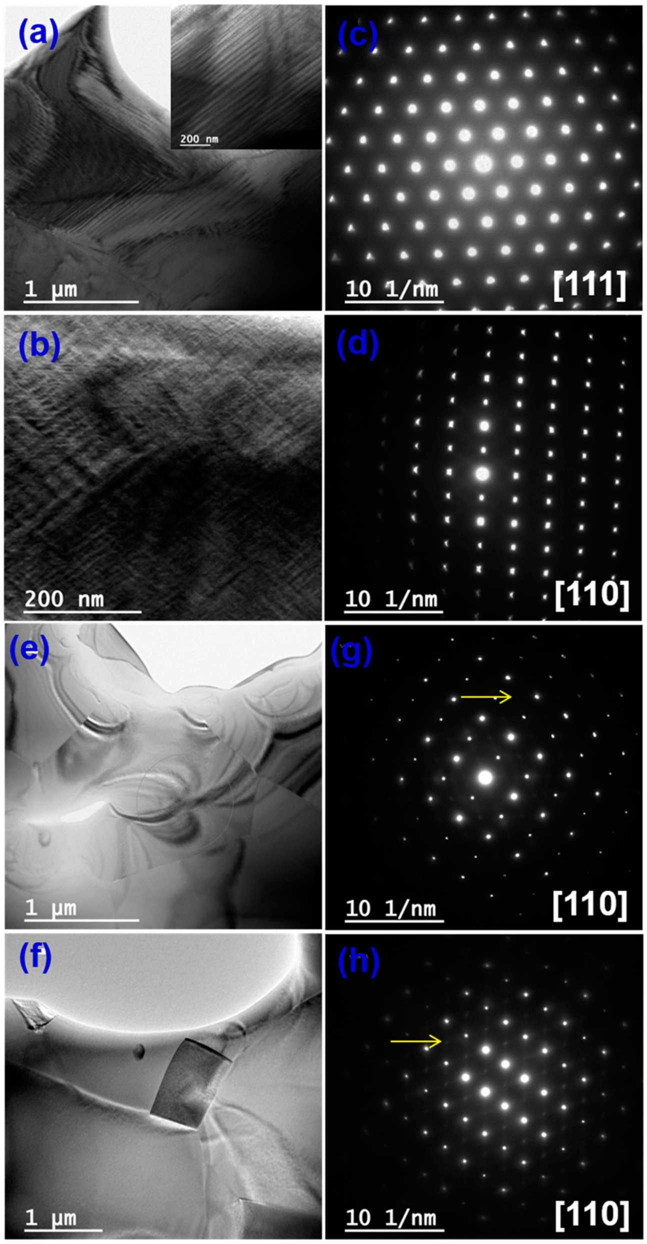

Figure 1. (a, b) Bright-field TEM images of domains in BCN; the magnified view of thin domains is depicted in the inset of (a). (c, d) SAED corresponding to the area presented in the inset of (a) and (b), respectively. (e, f) Bright-field TEM images of domains in SCN. (g, h) SAED corresponding to the area presented in (e) and (f). The arrows marked in (g) and (h) indicate superlattice reflections.

center positions in the AO_{12} dodecahedra leading to local polarization in the A-site of the perovskite structure.[25] Local distortions, resulting from substitution on the A-sites, cause the atoms around these sites to move away from the octahedral centers leading to nucleation of small polar clusters or regions.[26] However, in the case of SCN, we did not observe such small size domains in the TEM image. One can speculate that smaller ion substitution probably was not sufficient to provide enough distortions to nucleate domains in SCN.

The relative permittivity and Raman spectra of BCN and SCN are shown in Figure 2. In two prior studies, based on the high-temperature XRD results, the T_C of BCN was reported to be around ∼600 and ∼370 °C.[16,17] The Curie temperature of SCN was around 380 °C, and this material exhibited a giant dielectric constant with almost flat temperature-dependent dielectric behavior.[20,27] Figure 2a shows the temperature dependence of the relative permittivity of the BCN and SCN samples. The BCN sample sintered at 1250 °C had a peak at 350 °C where the phase transition temperature matched well with the one (T_C = 370 °C) reported by Venevtsev.[17] The maximum relative permittivity of BCN was about 39000, only half of the value reported by Zhang.[18] The peak value decreased to 10000, and the Curie temperature shifted to 400 °C, with increasing frequency from 1 to 100 kHz. The Curie temperature of the SCN sample (sintered at 1350 °C) was 390 °C, and the maximum relative permittivity was about 25000 at 1 kHz as shown in Figure 2a. For the SCN sample, the maximum value of the relative permittivity in this study was much higher than the previous results (<10000) reported by Bush,[27] and the phase transition temperature of the SCN sample agreed well with the one (T_C = 380 °C) reported by Dzhmukhadze.[20] The Curie temperature was also shifted to 410 °C with increasing frequency, and the minimum relative permittivity was around 10000 at 100 kHz.

Raman spectroscopy is a useful technique for detection of local structural changes in a system. For confirming the phase transition temperatures of BCN and SCN, Raman spectroscopy was employed, as shown in Figure 2b. The modes in the lower frequency regime have been attributed to the contribution from the A−O bond. However, the modes above 200 cm^{-1} can be attributed to the contributions from the BO_6 octahedra. The mode around 680 cm^{-1} in BCN gradually softened with temperature from 25 to 300 °C, and it disappeared at 400 °C as shown in Figure 2b. The softening of this mode indicates that the system is being driven toward phase transition.[28] These structural changes are consistent with the phase transition observed in temperature-dependent dielectric permittivity plots in the temperature range of 300−400 °C. Moreover, the broadening of the mode near 770 cm^{-1} in SCN was observed from 25 to 300 °C, and this mode also disappeared at 400 °C. The weak mode detected at 770 cm^{-1} at 300 °C is more conspicuous at 25 °C. However, this mode is absent at 400 °C for SCN, indicating its relation with the local octahedral distortions. On the basis of these results, it is believed that BCN and SCN had a phase transition around 300−400 °C, which is in agreement with T_C reported by Venevtsev[17] and Dzhmukhadze.[20]

2.3. High-Temperature Thermoelectric Properties of BCN and SCN.

Figure 3a shows the temperature dependence of the electrical conductivity for BCN and SCN samples. All of the values were less than 0.1 S/cm. The values for the BCN sample increased from 1.23×10^{-7} S/cm at room temperature and reached a saturated value of 0.07 S/cm at 600 °C. However, the SCN sample exhibited about 2 orders lower electrical conductivity of 1.87×10^{-9} S/cm at 75 °C, while the value increased significantly in the range 200−300 °C and started to saturate at ∼8.62×10^{-3} S/cm around 600 °C. The thermal conductivities as a function of temperature for BCN and SCN are shown in Figure 3b. All of the samples exhibited lower thermal conductivity from 1.2 to 2.1 W/m·K over a temperature range of 20−600 °C. The thermal conductivity values were found to linearly increase with increasing temperature. Because porous microstructures existed in the samples sintered at lower temperature (Figure S2), these BCN and SCN samples exhibited lower thermal conductivity values compared to more dense samples. Compared to the thermal

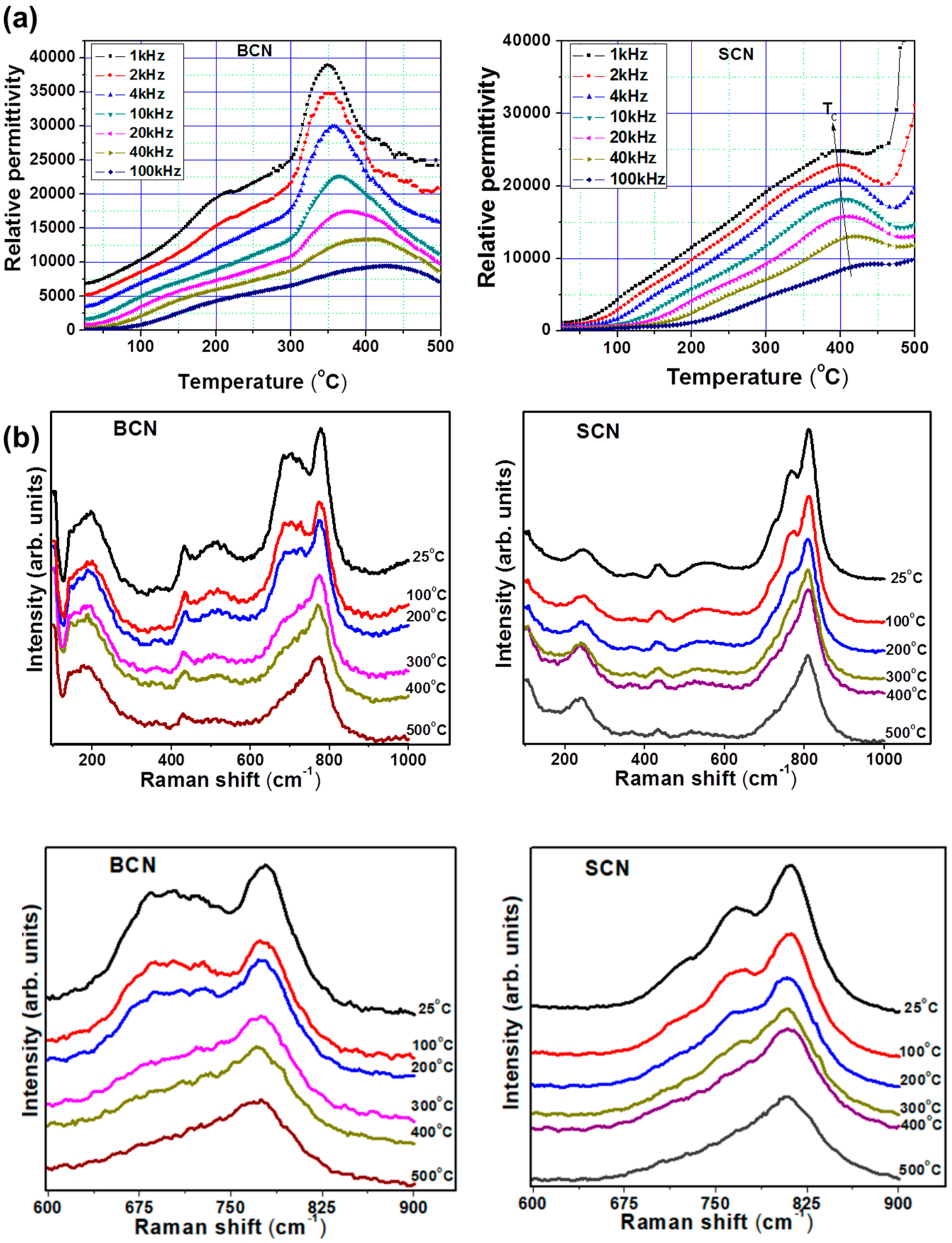

Figure 2. Temperature dependence of (a) relative permittivity and (b) Raman spectra for BCN and SCN.

conductivity values of SCN (1.5−2.1 W/m·K), BCN was found to exhibit lower thermal conductivity (1.2−1.6 W/m·K) due to increased phonon scattering facilitated by lower relative density. For these reasons, BCN and SCN ceramics have the potential to become candidates for high-temperature thermoelectric materials despite their low electrical conductivity in the low-temperature regime. Some preliminary results related to the thermoelectric measurements are provided in the Supporting Information.

The performance of a thermoelectric material is often characterized by the dimensionless figure of merit, *ZT*, which is defined as

$$ZT = \frac{S^2\sigma T}{k}$$

where S is the Seebeck coefficient, σ is the electrical conductivity, k is the thermal conductivity, and T is absolute temperature. Table 1 lists the high-temperature Seebeck coefficients and *ZT* values for the BCN and SCN samples. It is difficult to obtain continuous data below 400 °C by using our ZEM−3 measurement system due to high impedance of the samples in this range. The Seebeck coefficients for the BCN and SCN samples also show discontinuous and negative values, indicating n-type thermoelectric behavior, as shown in Table 1. The Seebeck coefficient values for the BCN samples

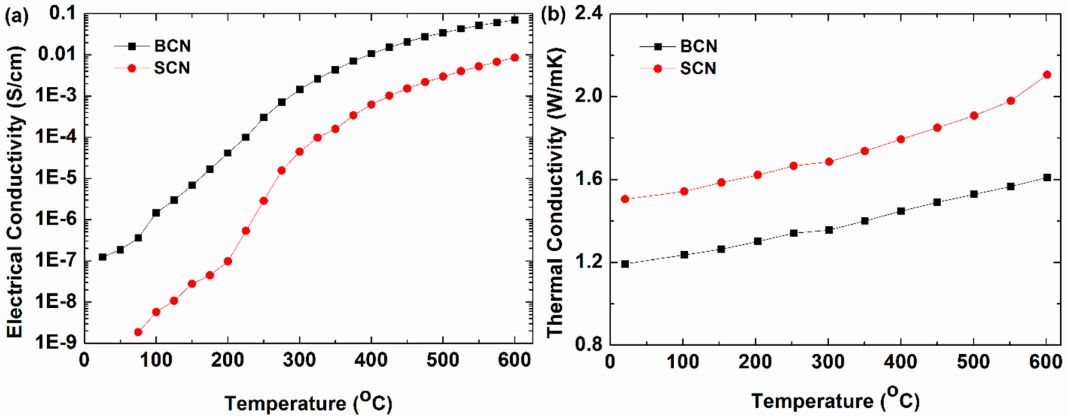

Figure 3. Temperature dependence of (a) electrical conductivity and (b) thermal conductivity for BCN and SCN.

Table 1. High-Temperature Seebeck Coefficients and *ZT* Values for the BCN and SCN Ceramics Fabricated by CS

sample	sintering temp (°C)	measuring temp (°C)	Seebeck coeff (μV/K)	*ZT* ($\times 10^{-4}$)
BCN	1200	400	−163	1.97
		500	−131	1.33
		600	−283	6.11
	1250	400	−143	0.43
		500	−134	0.47
		600	−152	0.78
SCN	1350	500	−441	3.98
		600	−399	4.16
	1400	400	−195	1.17
		500	−117	0.42
		600	−329	3.36

were in the range between −131 and −283 μV/K in the high-temperature range. However, the SCN samples show randomly distributed Seebeck coefficients from −117 to −441 μV/K for the samples fabricated by CS in the range 400−600 °C. The *ZT* for the BCN samples were quite low values and in the range of 4.32×10^{-5}–6.11×10^{-4} at high temperatures, as shown in Table 1. The SCN samples also exhibited small *ZT* values in the range of 4.22×10^{-5}–4.16×10^{-4} at high temperatures due to their low electrical conductivity. While the observed *ZT* values here are small, this work can be extended to modified BCN and SCN systems with nanoinclusions of various metals to compensate for their low electrical conductivity to achieve a higher *ZT* value.

2.4. Terahertz Frequency Domain Spectroscopy and Phonon Mode Dynamics in BCN and SCN. Phonon dynamics play an important role in thermal conductivity of the material. Therefore, high-resolution terahertz (THz) frequency domain spectroscopy was employed to discover phonon modes and structural transformations in BCN and SCN systems.[29] The absorption coefficient α and refractive index n for the BCN and SCN samples were extracted through THz measurements with increasing temperature up to 600 °C, as shown in Figure 4a,b. The details of the calculations can be found in ref 29. We observed two phonon modes at 0.30 and 0.95 THz at 50 °C for the 30 μm BCN sample and two phonon modes at 0.17 and 1.1 THz at room temperature for the 60 μm SCN sample. The reproducible results (five different samples) were obtained through THz measurements, and the observed phonon modes were not affected by the temperature cycling. In the absorption spectra, peak positions for both BCN and SCN materials did not change with temperature, denying the presence of a soft mode responsible for the structural change in these materials up to 600 °C.

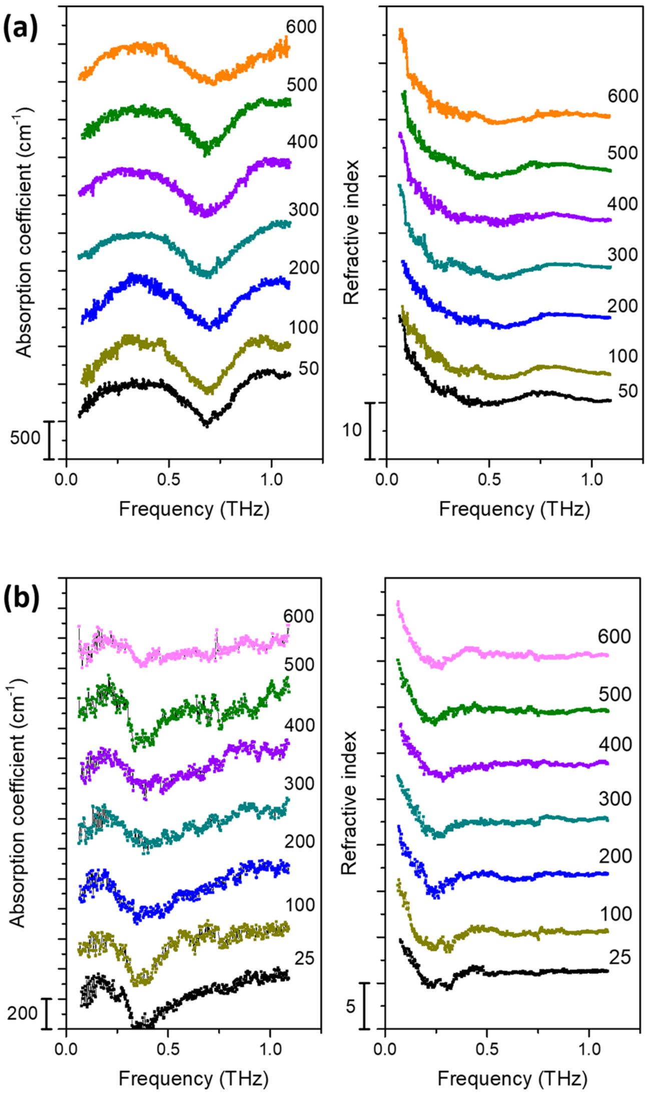

Figure 4. THz absorption and refractive index of (a) BCN and (b) SCN ceramic materials recorded at various temperature. The labels inside the plot refer to the sample temperature in Celsius.

In terms of thermal transport, optical phonon modes with frequencies lower than 1.12 THz (37.36 cm^{-1}) can effectively scatter acoustic phonons carrying heat, which hinders the phonon transport of heat.[31] The appearance of optical modes and strong anharmonic phonon scattering[32] can account for low thermal conductivity values observed in BCN and SCN, as shown in Figure 3b. Two phonon modes were observed at 0.30 and 0.95 THz in BCN, and at 0.17 and ∼1 THz in SCN materials. The thermal conductivity of BCN was lower than the value of SCN over the entire temperature range due to this broad spectrum of phonon frequencies in BCN. The THz measurements results were in good agreement with the thermal conductivity results (Figure 3b).

Acharya et al. reported that the Raman intensity of peak increases at phase transition temperature (for Ag_8SnGe_6), and the intensity decreases gradually and merges with vibrational modes at higher temperature in the cubic phase.[33] According to Dutta and Matteppanavar's research, in TlSe thermoelectric material, the caged intrinsic Tl^+ rattler results in additional channels for phonon scattering which corresponds to the lowest frequency optical modes in room temperature THz time domain spectroscopy and temperature-dependent Raman spectroscopy.[34] We expected to find structural transformations in BCN and SCN through THz frequency domain spectroscopy, but we could not find any signature of phase transition.

3. CONCLUSIONS

We synthesized perovskite-type $Ba(Cu_{1/3}Nb_{2/3})O_3$ and $Sr(Cu_{1/3}Nb_{2/3})O_3$ ceramics using a conventional solid state reaction method. The relative permittivity analysis and Raman spectra of $Ba(Cu_{1/3}Nb_{2/3})O_3$ and $Sr(Cu_{1/3}Nb_{2/3})O_3$ indicated the presence of a phase transition in the temperature range of 300−400 °C. We further demonstrated that $Ba(Cu_{1/3}Nb_{2/3})O_3$ and $Sr(Cu_{1/3}Nb_{2/3})O_3$ have a different microstructure based on TEM analysis. $Ba(Cu_{1/3}Nb_{2/3})O_3$ exhibited nanodomain structures, however, without macroscale ferroelectric responses. On the other hand, by substituting smaller Sr on the Ba-site, these nanoscale domains disappeared in $Sr(Cu_{1/3}Nb_{2/3})O_3$. Interestingly, $Sr(Cu_{1/3}Nb_{2/3})O_3$ exhibited superlattice reflections in electron diffraction patterns, signifying B-site ordering or octahedra tilting. The THz spectroscopy results indicated the presence of two low-frequency modes in both of the samples, which were temperature independent. The electrical and thermal properties and the phonon mode dynamics of $Ba(Cu_{1/3}Nb_{2/3})O_3$ and $Sr(Cu_{1/3}Nb_{2/3})O_3$ were investigated for the first time in this work. The fundamental understanding developed in this work is expected to guide future research of efficient high-temperature oxide thermoelectric materials.

4. EXPERIMENTAL SECTION

4.1. Sample Preparation. The BCN and SCN samples were prepared by the traditional solid state reaction method. Powders of $BaCO_3$, $SrCO_3$, CuO, and Nb_2O_5 were combined in their stoichiometric ratios and ball milled for 24 h. The mixed powders were calcined at 800 °C for 2 h and 900 °C for 2 h in air with an intermediate grinding procedure and then uniaxially pressed into pellets of 12 mm diameter and 1−2 mm thickness. All pellets were sintered by conventional sintering at temperatures in the range 1150−1400 °C for 2 h.

4.2. Material Characterization Techniques. X-ray diffraction (XRD; Bruker D8 diffractometer) spectroscopy was performed to identify the crystalline phases. Micrographs of various samples were recorded by using field emission scanning electron microscopy (FESEM; LEO (Zeiss) 1550 field-emission) as well as with transmission electron microscopy (TEM; JEOL 2100) operated at 200 kV. Silver electrodes were applied on the top and bottom of the sintered pellets for electrical measurements. The dielectric response as a function of temperature at various frequencies was measured by using an impedance analyzer (HP 4292A, oscillation level of 500 mV) coupled with a high-temperature oven. Raman studies were conducted in the backscattering geometry using a Raman spectrometer (Jobin-Yvon LabRam HR 800 high-resolution instrument, laser radiation of 514.5 nm from a Coherent Innova 99 argon source). The green laser light was focused to an ∼2 μm diameter by using a Raman microprobe with a 50× objective. The densities of the sintered ceramic samples were measured by Archimedes' method. The thermal diffusivity and specific heat measurements were performed by using a laser flash system (ULVAC-RIKO TC-1200RH). A disk-shaped sample of about 10 mm diameter and 1 mm thickness was used for evaluating thermal conductivity. The thermal conductivity, κ, was calculated from $\kappa = \alpha\rho C_p$, where α is thermal diffusivity, ρ is density, and C_p is the specific heat. The THz spectra were recorded by using a commercial vector network analyzer (Agilent N5225A PNA, 10 MHz−50 GHz) and THz frequency extenders together with matched harmonic detectors (Virginia Diodes, Inc., 60 GHz−1.12 THz). The details of the THz measurement are described in refs 29 and 30.

■ ASSOCIATED CONTENT

Supporting Information

The Supporting Information is available free of charge at https://pubs.acs.org/doi/10.1021/acsaem.0c00342.

> XRD patterns of BCN and SCN ceramics; FESEM images of BCN and SCN ceramics; crystalline structure of $A(Cu_{1/3}Nb_{2/3})O_3$ (A = Ba, Sr); second harmonic generation (SHG) from $K_{0.5}Na_{0.5}NbO_3$ (KNN) reference sample, SCN powder, and BCN powder; and preliminary results related to the thermoelectric measurements (PDF)

■ AUTHOR INFORMATION

Corresponding Authors

Myung-Eun Song − *Center for Energy Harvesting Materials and Systems (CEHMS) and Department of Materials Science and Engineering, Virginia Tech, Blacksburg, Virginia 24061, United States;* orcid.org/0000-0002-2204-9476; Email: songme@vt.edu

N. Q. Vinh − *Department of Physics and Center for Soft Matter and Biological Physics, Virginia Tech, Blacksburg, Virginia 24061, United States;* orcid.org/0000-0002-3071-1722; Email: vinh@vt.edu

Shashank Priya − *Department of Materials Science and Engineering, Pennsylvania State University, University Park, Pennsylvania 16802, United States;* Email: sup103@psu.edu

Authors

Deepam Maurya − *Department of Materials Science and Engineering, Virginia Tech, Blacksburg, Virginia 24061, United States; Intel Corporation, Chandler, Arizona 85248, United States*

Yifei Wang − *Department of Physics and Center for Soft Matter and Biological Physics, Virginia Tech, Blacksburg, Virginia 24061, United States*

Jue Wang − *Department of Mechanical Engineering, Virginia Tech, Blacksburg, Virginia 24061, United States*

Min-Gyu Kang − *Department of Materials Science and Engineering, Pennsylvania State University, University Park,* *Pennsylvania 16802, United States;* orcid.org/0000-0001-9247-6476

David Walker − *Department of Physics, University of Warwick, Coventry CV4 7AL, United Kingdom;* orcid.org/0000-0002-8583-4279

Pam A. Thomas − *Department of Physics, University of Warwick, Coventry CV4 7AL, United Kingdom*

Scott T. Huxtable − *Department of Mechanical Engineering, Virginia Tech, Blacksburg, Virginia 24061, United States*

Robert J. Bodnar − *Department of Geosciences, Virginia Tech, Blacksburg, Virginia 24061, United States*

Complete contact information is available at: https://pubs.acs.org/10.1021/acsaem.0c00342

Notes

The authors declare no competing financial interest.

■ ACKNOWLEDGMENTS

The authors acknowledge support from the DARPA MATRIX program. M.-G.K. thanks AFOSR through Grant FA9550-14-1-0376 (Ali Sayir). D.M. thanks AMRDEC for support through the SBIR program. S.P. acknowledges the support from NSF-CREST through Grant HRD 1547771.

■ REFERENCES

(1) Elliott, D. A balancing act for renewables. *Nat. Energy* **2016**, *1*, 15003.

(2) Suberu, M. Y.; Mustafa, M. W.; Bashir, N. Energy storage systems for renewable energy power sector integration and mitigation of intermittency. *Renewable Sustainable Energy Rev.* **2014**, *35*, 499−514.

(3) Chu, S.; Majumdar, A. Opportunities and challenges for a sustainable energy future. *Nature* **2012**, *488*, 294−303.

(4) Götz, M.; Lefebvre, J.; Mörs, F.; Koch, A. M.; Graf, F.; Bajohr, S.; Reimert, R.; Kolb, T. Renewable Power-to-Gas: A technological and economic review. *Renewable Energy* **2016**, *85*, 1371−1390.

(5) Tan, P.; Liu, M. L.; Shao, Z. P.; Ni, M. Recent Advances in Perovskite Oxides as Electrode Materials for Nonaqueous Lithium−Oxygen Batteries. *Adv. Energy Mater.* **2017**, *7*, 1602674.

(6) Zhang, W.; Eperon, G. E.; Snaith, H. J. Metal halide perovskites for energy applications. *Nat. Energy* **2016**, *1*, 16048.

(7) Zhu, L.; Liu, Y.; Su, C.; Zhou, W.; Liu, M. L.; Shao, Z. P. Perovskite $SrCo_{0.9}Nb_{0.1}O_{3-\delta}$ as an Anion-Intercalated Electrode Material for Supercapacitors with Ultrahigh Volumetric Energy Density. *Angew. Chem., Int. Ed.* **2016**, *55*, 9576−9679.

(8) Zhu, L.; Ran, R.; Tade, M.; Wang, W.; Shao, Z. P. Perovskite materials in energy storage and conversion. *Asia-Pac. J. Chem. Eng.* **2016**, *11*, 338−369.

(9) Jung, H. S.; Park, N. G. Perovskite Solar Cells: From Materials to Devices. *Small* **2015**, *11*, 10−25.

(10) West, A. R. Basic Solid State Chemistry. In *Electrical Properties*; John Wiley & Sons: Chichester, 2000; Chapter 7, pp 293−372.

(11) Davies, P. K.; Wu, H.; Borisevich, A. Y.; Molodetsky, I. E.; Farber, L. Crystal Chemistry of Complex Perovskites: New Cation-Ordered Dielectric Oxides. *Annu. Rev. Mater. Res.* **2008**, *38*, 369−401.

(12) Park, H.-B.; Huh, H.; Kim, S.-J. Structure and Bonding of Perovskites $A(Cu_{1/3}Nb_{2/3})O_3$ (A = Sr, Ba and Pb) and Their Series of Mixed Perovskites. *Bull. Korean Chem. Soc.* **1992**, *13*, 122−127.

(13) Shannon, R. D. Revised effective ionic radii and systematic studies of interatomic distances in halides and chalcogenides. *Acta Crystallogr., Sect. A: Cryst. Phys., Diffr., Theor. Gen. Crystallogr.* **1976**, *32*, 751−767.

(14) Qi, T.; Grinberg, I.; Rappe, A. M. Correlations between tetragonality, polarization, and ionic displacement in PbTiO3-derived ferroelectric perovskite solid solutions. *Phys. Rev. B: Condens. Matter Mater. Phys.* **2010**, *82*, 134113.

(15) Jahn, H. A.; Teller, E. Stability of polyatomic molecules in degenerate electronic states - I—Orbital degeneracy. *Proc. R. Soc. London, Ser. A* **1937**, *161*, 220−235.

(16) Priya, S.; Ando, A.; Sakabe, Y. Nonlead perovskite materials: $Ba(Li_{1/4}Nb_{3/4})O_3$ and $Ba(Cu_{1/3}Nb_{2/3})O_3$. *J. Appl. Phys.* **2003**, *94*, 1171−1177.

(17) Venevtsev, Y. N. Ferroelectric family of barium titanate. *Mater. Res. Bull.* **1971**, *6*, 1085−1096.

(18) Zhang, W.; Kumada, N.; Yonesaki, Y.; Takei, T.; Kinomura, N.; Hayashi, T.; Azuma, M.; Takano, M. Ferroelectric perovskite-type barium copper niobate: $BaCu_{1/3}Nb_{2/3}O_3$. *J. Solid State Chem.* **2006**, *179*, 4052−4055.

(19) Blasse, G. Vibrational spectra of solid solution series with ordered perovskite structure. *J. Inorg. Nucl. Chem.* **1975**, *37*, 1347−1351.

(20) Dzhmukhadze, D. F.; Venevtsev, Y. N.; Zhdanov, G. S. Investigation into the $PbTiO_3$-SrCusub(1/3)Nbsub(2/3)O_3 system. *Kristallografiya* **1971**, *16*, 172−176.

(21) Rao, K. S.; Rao, P. S. J.; Rao, K. R.; Rao, A. V. P.; Robin, A. I.; Tandon, R. P. Dielectric and conductivity properties of lanthanum-modified strontium copper niobate. *J. Mater. Sci. Lett.* **1994**, *13*, 253−255.

(22) Salje, E. K. H.; Hayward, S. A.; Lee, W. T. Ferroelastic phase transitions. *Acta Crystallogr., Sect. A: Found. Crystallogr.* **2005**, *61*, 3−18.

(23) Galasso, F.; Katz, L.; Ward, R. Substitution in the Octahedrally Coördinated Cation Positions in Compounds of the Perovskite Type^{1,2}. *J. Am. Chem. Soc.* **1959**, *81*, 820−823.

(24) Galasso, F.; Darby, W. Ordering of the octahedrally coördinated cation position in the perovskite structure. *J. Phys. Chem.* **1962**, *66*, 131−132.

(25) Shimizu, T.; Fu, D.; Taniguchi, H.; Taniyama, T.; Itoh, M. Origin of the dielectric response in $Ba_{0.767}Ca_{0.233}TiO_3$. *Appl. Phys. Lett.* **2012**, *100*, 102908.

(26) Waeselmann, N.; Mihailova, B.; Maier, B. J.; Paulmann, C.; Gospodinov, M.; Marinova, V.; Bismayer, U. Local structural phenomena in pure and Ru-doped $0.9PbZn_{1/3}Nb_{2/3}O_3$ - $0.1PbTiO_3$ near the morphotropic phase boundary as revealed by Raman spectroscopy. *Phys. Rev. B: Condens. Matter Mater. Phys.* **2011**, *83*, 214104.

(27) Bush, A. A.; Sirotinkin, V. P. Dielectric properties of $Sr_3CuNb_2O_9$ perovskite ceramics. *Inorg. Mater.* **2008**, *44*, 1233−1239.

(28) Maurya, D.; Kumar, A.; Petkov, V.; Mahaney, J. E.; Katiyar, R. S.; Priya, S. Local structure and piezoelectric instability in lead-free (1 - X)$BaTiO_3$-xA$(Cu_{1/3}Nb_{2/3})O_3$ (A = Sr, Ca, Ba) solid solutions. *RSC Adv.* **2014**, *4*, 1283−1292.

(29) Maurya, D.; Charkhesht, A.; Nayak, S. K.; Sun, F.-C.; George, D.; Pramanick, A.; Kang, M.-G.; Song, H.-C.; Alexander, M. M.; Lou, D.; Khodaparast, G. A.; Alpay, S. P.; Vinh, N. Q.; Priya, S. Soft phonon mode dynamics in Aurivillius-type structures. *Phys. Rev. B: Condens. Matter Mater. Phys.* **2017**, *96*, 134114.

(30) George, D. K.; Charkhesht, A.; Vinh, N. Q. New terahertz dielectric spectroscopy for the study of aqueous solutions. *Rev. Sci. Instrum.* **2015**, *86*, 123105.

(31) Roychowdhury, S.; Jana, M. K.; Pan, J.; Guin, S. N.; Sanyal, D.; Waghmare, U. V.; Biswas, K. Soft Phonon Modes Leading to Ultralow Thermal Conductivity and High Thermoelectric Performance in AgCuTe. *Angew. Chem., Int. Ed.* **2018**, *57*, 4043−4047.

(32) Zhao, L.-D.; Lo, S.-H.; Zhang, Y.; Sun, H.; Tan, G.; Uher, C.; Wolverton, C.; Dravid, V. P.; Kanatzidis, M. G. Ultralow thermal conductivity and high thermoelectric figure of merit in SnSe crystals. *Nature* **2014**, *508*, 373−377.

(33) Acharya, S.; Pandey, J.; Soni, A. Enhancement of Power Factor for Inherently Poor Thermal Conductor Ag_8GeSe_6 by Replacing Ge with Sn. *ACS Appl. Energy Mater.* **2019**, *2*, 654−660.

(34) Dutta, M.; Matteppanavar, S.; Prasad, M. V. D.; Pandey, J.; Warankar, A.; Mandal, P.; Soni, A.; Waghmare, U. V.; Biswas, K. Ultralow Thermal Conductivity in Chain-like TlSe Due to Inherent Tl^+ Rattling. *J. Am. Chem. Soc.* **2019**, *141*, 20293−20299.

Supporting Information

Phase Transitions and Phonon Mode Dynamics of $Ba(Cu_{1/3}Nb_{2/3})O_3$ and $Sr(Cu_{1/3}Nb_{2/3})O_3$ for Understanding Thermoelectric Response

Myung-Eun Song[1, 2, *], Deepam Maurya[2, 8], Yifei Wang[3], Jue Wang[4], Min-Gyu Kang[6], David Walker[7], Pam A. Thomas[7], Scott T. Huxtable[4], Robert J. Bodnar[5], N. Q. Vinh[3, *], and Shashank Priya[6, *]

[1]*Center for Energy Harvesting Materials and Systems (CEHMS), Virginia Tech, Blacksburg, Virginia 24061, United States*

[2]*Department of Materials Science and Engineering, Virginia Tech, Blacksburg, Virginia 24061, United States*

[3]*Department of Physics and Center for Soft Matter and Biological Physics, Virginia Tech, Blacksburg, Virginia 24061, United States*

[4]*Department of Mechanical Engineering, Virginia Tech, Blacksburg, Virginia 24061, United States*

[5]*Department of Geosciences, Virginia Tech, Blacksburg, Virginia 24061, United States*

[6]*Department of Materials Science and Engineering, Pennsylvania State University, University Park, Pennsylvania 16802, United States*

[7]*Department of Physics, University of Warwick, Coventry CV4 7AL, United Kingdom*

[8]*Intel Corporation, Chandler, Arizona 85248, United States*

[*]E-mail: *songme@vt.edu*

[*]E-mail: *vinh@vt.edu*

[*]E-mail: *sup103@psu.edu*

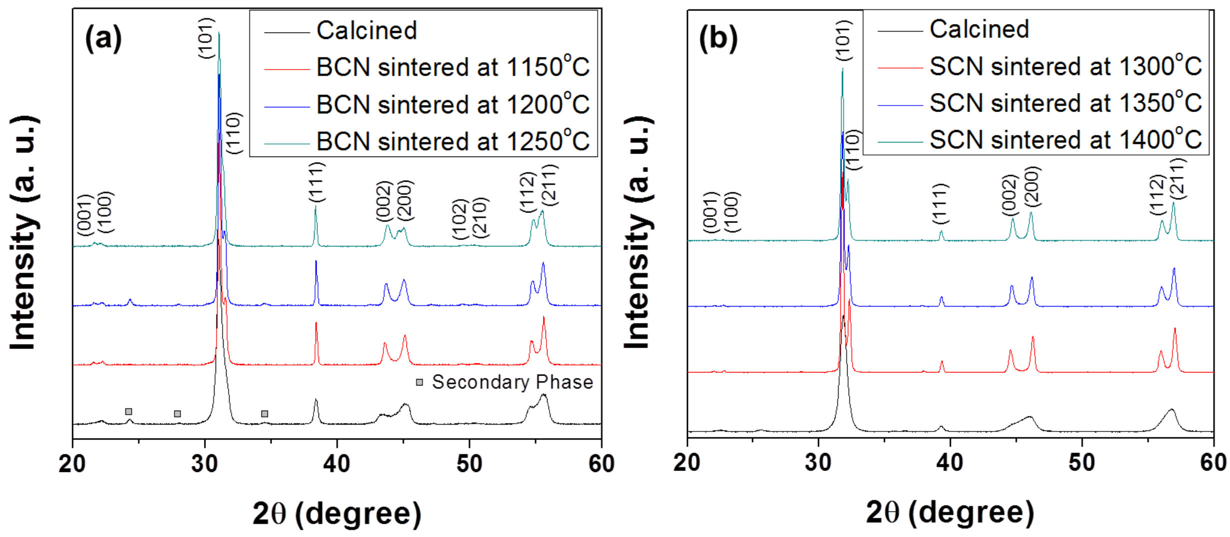

Figure S1. XRD patterns of (a) Ba($Cu_{1/3}Nb_{2/3}$)O_3 (BCN) and (b) Sr($Cu_{1/3}Nb_{2/3}$)O_3 (SCN) ceramics calcined and sintered at various temperatures for 2 h.

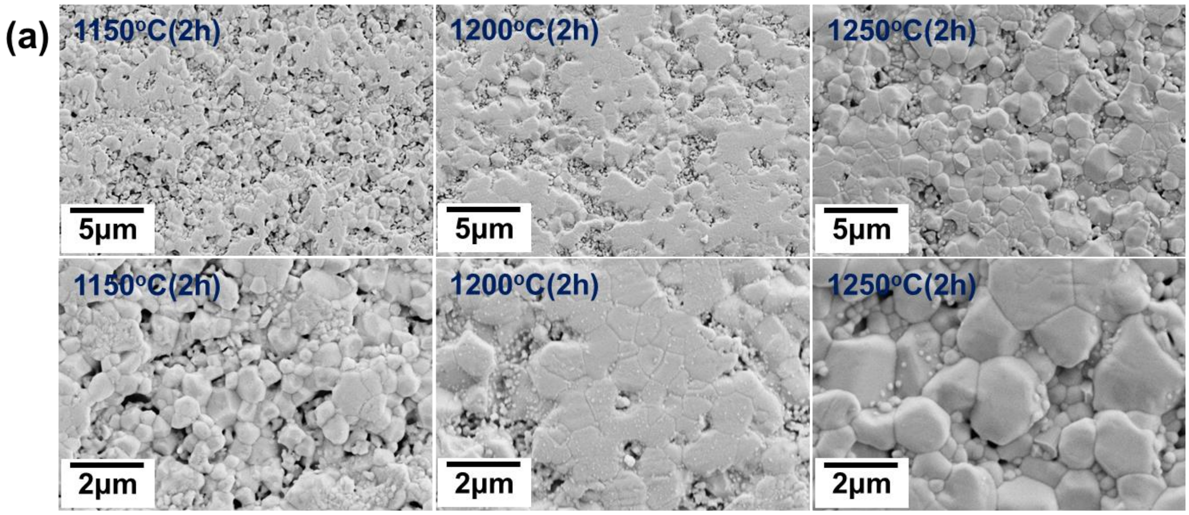

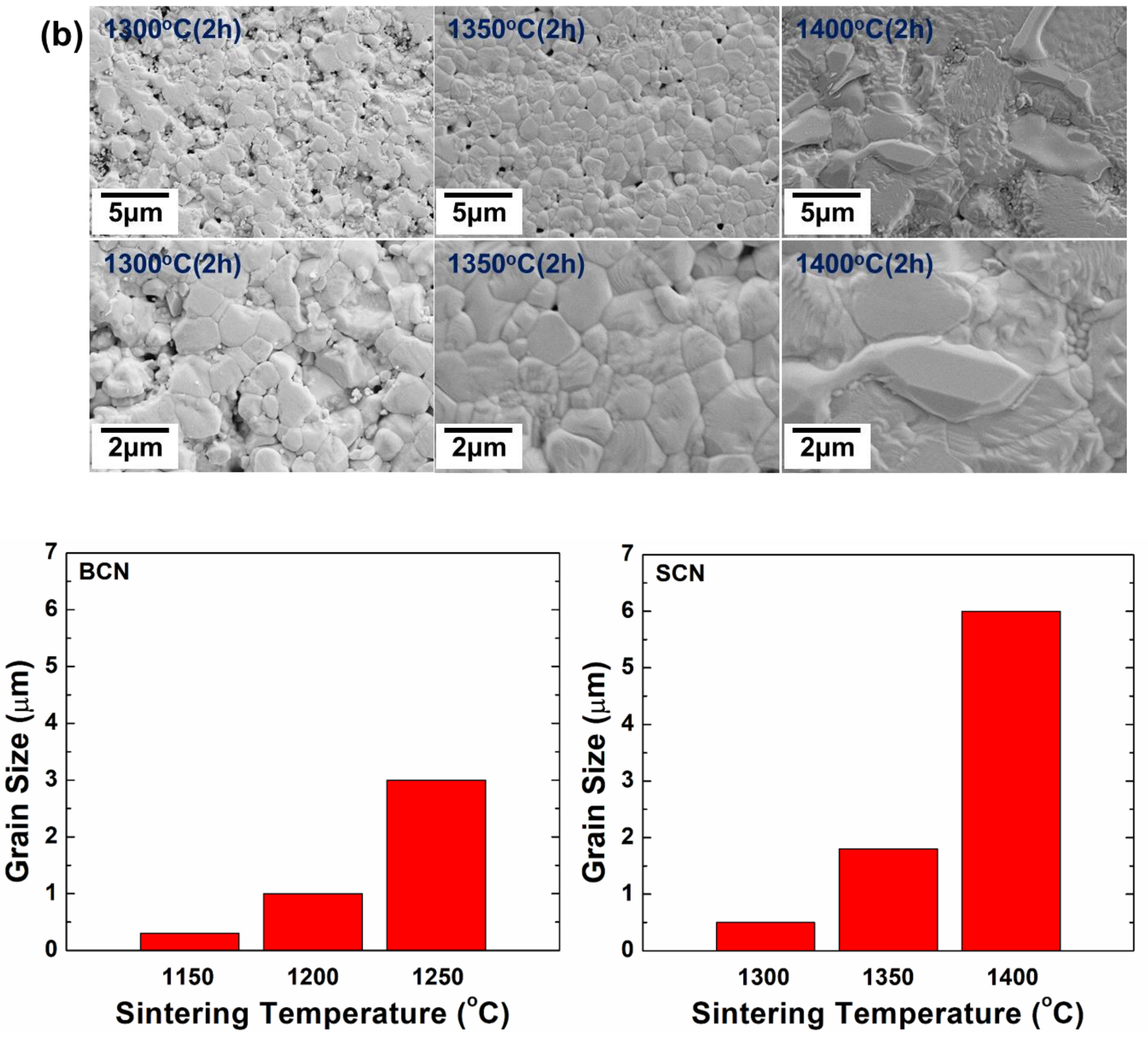

Figure S2. FESEM images of (a) $Ba(Cu_{1/3}Nb_{2/3})O_3$ (BCN) and (b) $Sr(Cu_{1/3}Nb_{2/3})O_3$ (SCN) ceramics sintered at various temperatures for 2 h. The histogram refers to the grain sizes in both the samples.

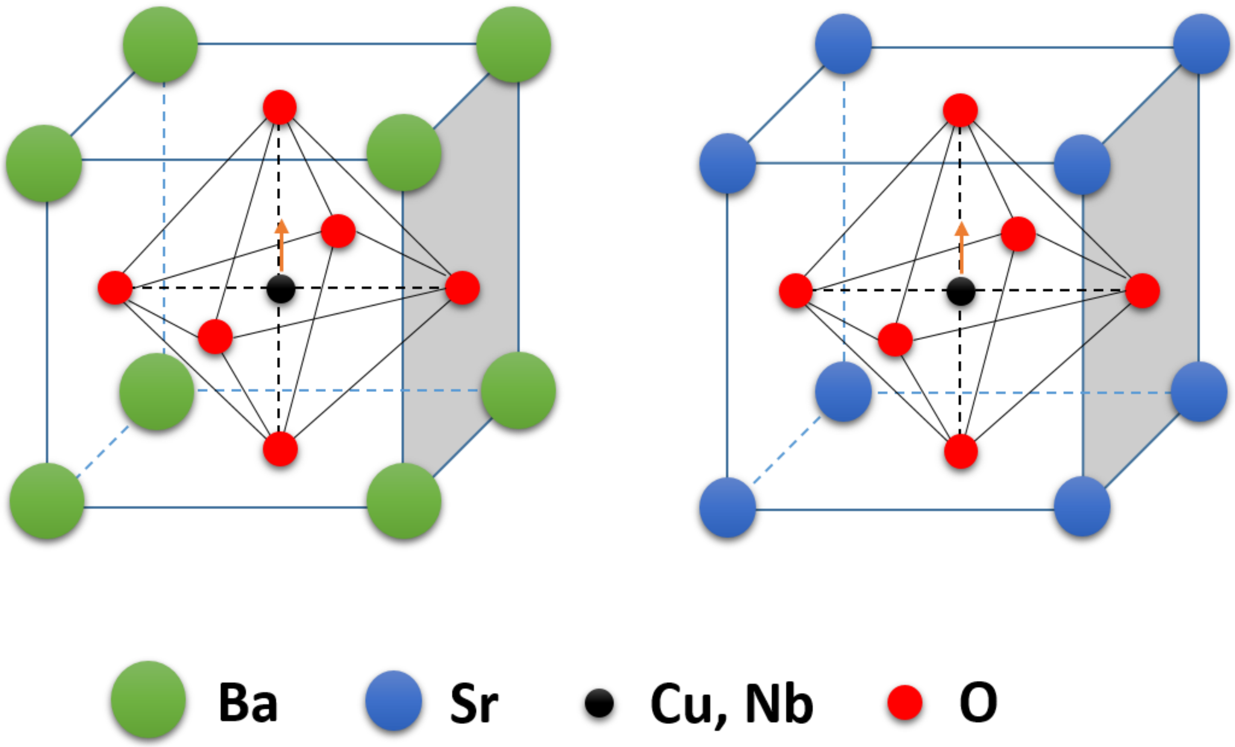

Figure S3. Schematic view of the crystalline structure of $A(Cu_{1/3}Nb_{2/3})O_3$ (A=Ba, Sr) and partial substitution of Ba/Sr on A sites in the perovskite structure. The displacement of A sites and 1:2-repeated Cu and Nb cation sites are omitted for clarity.

SCN / BCN powders - Second Harmonic Generation (SHG)

Second Harmonic Generation (SHG) measurements were undertaken using a pulsed Nd:YAG laser (1064nm). The powders were mounted in between two cover slips surrounded by a plastic washer, with a thickness of 1 mm. The fundamental was recorded by splitting the beam and using a photodiode. The SHG signal was measured using a photomultiplier tube with filters to prevent the fundamental from being detected – no signal was detected in the photomultiplier tube if no sample was present in the beampath. The laser was pulsed at 1 Hz and up to 500 repeat iterations were collected and averaged mathematically. A $K_{0.5}Na_{0.5}NbO_3$ (KNN) reference sample was used to calibrate the system to have a strong SHG signal.

Figure S4 shows the results of the SHG patterns. The KNN shows a clear signal at the same laser power settings and conditions. The SCN and BCN powders do not show any evidence of a second harmonic signal above the background in an average over 500 iterations. However, this result does not imply that the material must be centrosymmetric, as it is only the signal that confirms it must be non-centrosymmetric. The samples may either a) be centrosymmetric b) have a very weak non-linear optical response so that the peak is below the detectable threshold, or c) be strongly absorbing in either the infrared or green wavelengths.

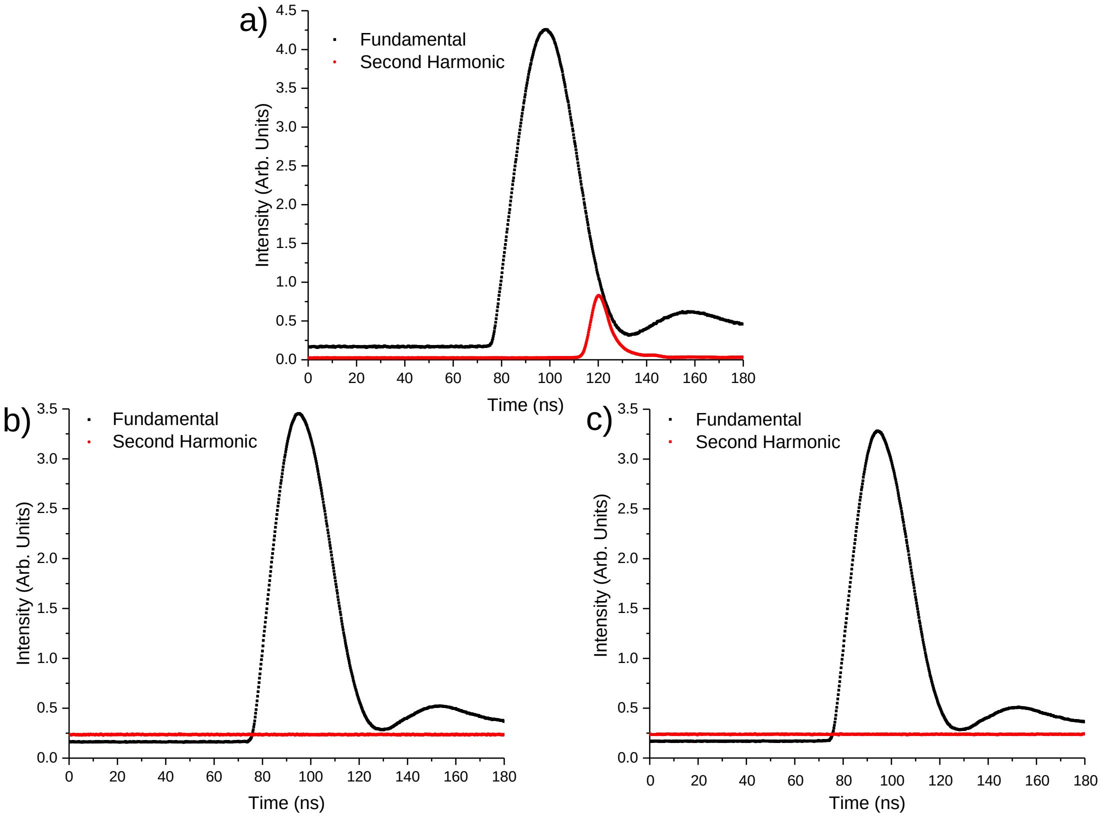

Figure S4. SHG from a) KNN reference sample b) SCN powder c) BCN powder. Neither the SCN nor BCN powders show a detectable second harmonic signal over 500 iterations.

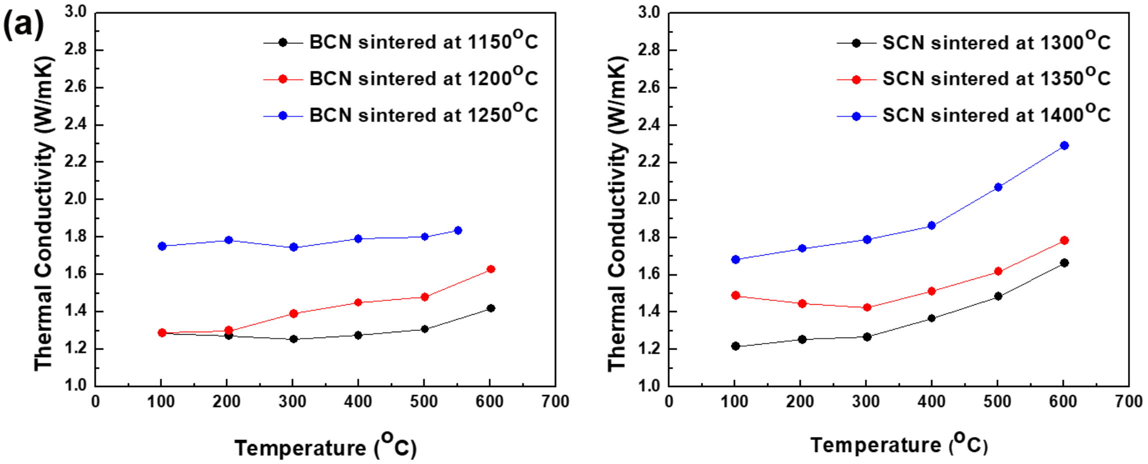
(a)
Thermal Conductivity (W/mK)
3.0
2.8
2.6
2.4
2.2
2.0
1.8
1.6
1.4
1.2
1.0
0
100
200
300
400
500
600
700
Temperature (°C)
BCN sintered at 1150°C
BCN sintered at 1200°C
BCN sintered at 1250°C
SCN sintered at 1300°C
SCN sintered at 1350°C
SCN sintered at 1400°C

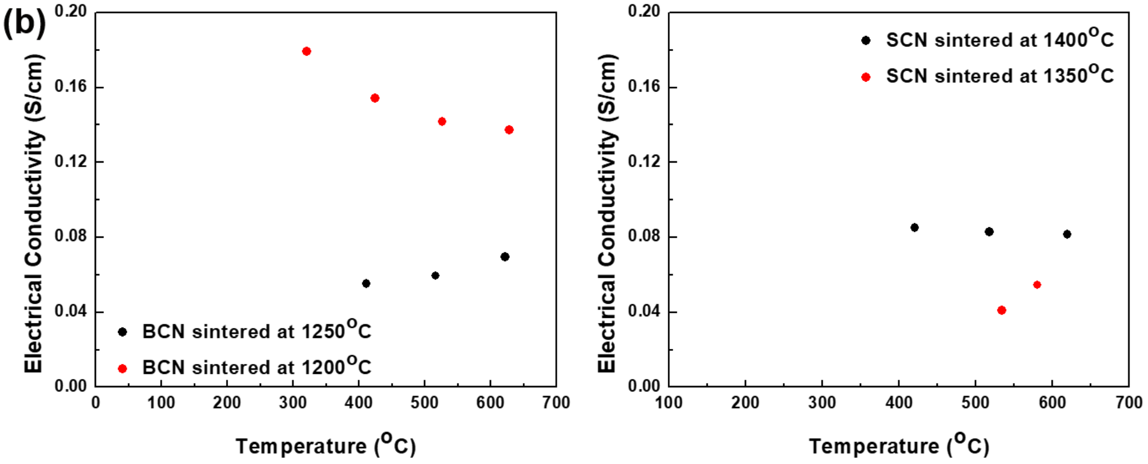
(b)
Electrical Conductivity (S/cm)
0.20
0.16
0.12
0.08
0.04
0.00
0
100
200
300
400
500
600
700
Temperature (°C)
BCN sintered at 1250°C
BCN sintered at 1200°C
SCN sintered at 1400°C
SCN sintered at 1350°C

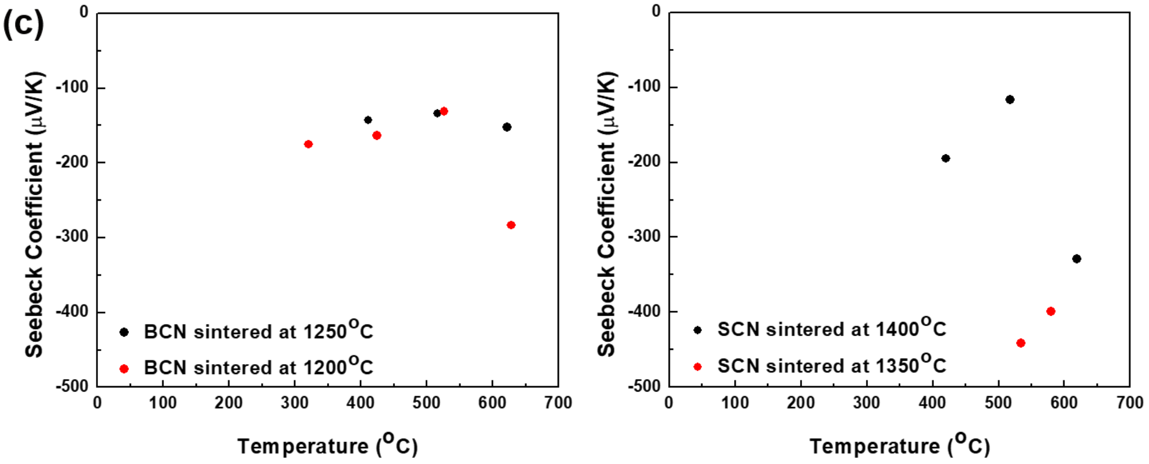
(c)
Seebeck Coefficient (μV/K)
0
-100
-200
-300
-400
-500
0
100
200
300
400
500
600
700
Temperature (°C)
BCN sintered at 1250°C
BCN sintered at 1200°C
SCN sintered at 1400°C
SCN sintered at 1350°C

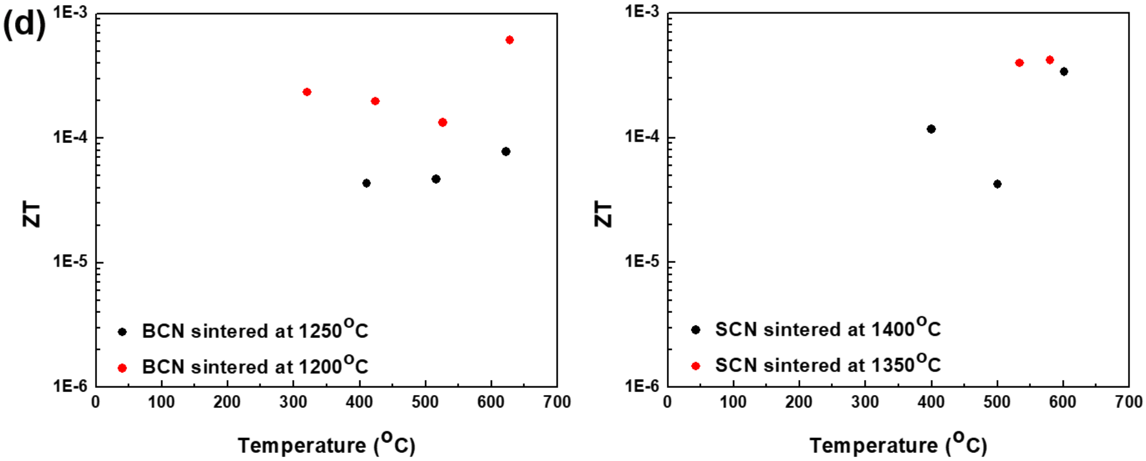

Figure S5. The (a) thermal conductivity, (b) electrical conductivity, (c) Seebeck coefficient, and (d) *ZT* of $Ba(Cu_{1/3}Nb_{2/3})O_3$ (BCN) and $Sr(Cu_{1/3}Nb_{2/3})O_3$ (SCN) ceramics sintered at various temperatures for 2 h.